ACS Partner Journal

Journal of the American Society for Mass Spectrometry

pubs.acs.org/jasms

Research Article

Electron Driven Reactions in Tetrafluoroethane: Positive and Negative Ion Formation

João Pereira-da-Silva, Rodrigo Rodrigues, João Ramos, Carlos Brígido, Alexandru Botnari, Miguel Silvestre, João Ameixa, Mónica Mendes, Fábio Zappa, Stephen J. Mullock, João M. M. Araújo, Márcio T. do N. Varella, Lucas M. Cornetta,* and Filipe Ferreira da Silva*

Cite This: *J. Am. Soc. Mass Spectrom.* 2021, 32, 1459−1468

Read Online

ACCESS | Metrics & More | Article Recommendations | Supporting Information

ABSTRACT: In the search for alternatives to chlorine-containing gases, tetrafluoroethane, CF_3CH_2F (R134a), a widely used refrigerant gas, has been recognized as a promising substitute for dichlorodifluoromethane, CCl_2F_2 (R12). When R12 is replaced by R134a, the global warming potential drops from 8100 to 1430, the ozone depletion potential changes from 1 to 0, and the atmospheric lifetime decreases from 100 to 14 years. Electron interactions in the gas phase play a fundamental role in the atmospheric sciences. Here, we present a detailed study on electron-driven fragmentation pathways of CF_3CH_2F, in which we have investigated processes induced by both electron ionization and electron attachment. The measurements allow us to report the ion efficiency curves for ion formation in the energy range of 0 up to 25 eV. For positive ion formation, R134a dissociates into a wide assortment of ions, in which CF_3^+ is observed as the most abundant out of seven ions with a relative intensity above 2%. The results are supported by quantum chemical calculations based on bound state techniques, electron-impact ionization models, and electron-molecule scattering simulations, showing a good agreement. Moreover, the experimental first ionization potential was found at 13.10 ± 0.17 eV and the second at around 14.25 eV. For negative ion formation, $C_2F_3^-$ was detected as the only anion formed, above 8.3 eV. This study demonstrates the role of electrons in the dissociation of R134a, which is relevant for an improvement of the refrigeration processes as well as in atmospheric chemistry and plasma sciences.

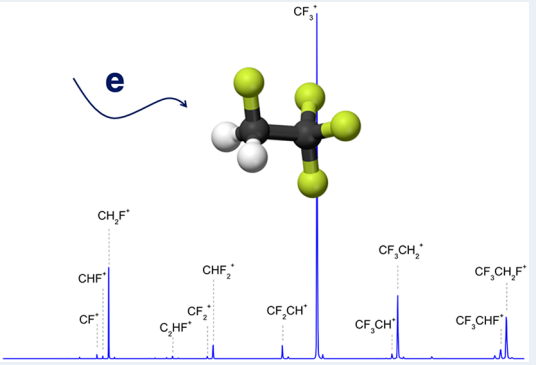

INTRODUCTION

Since the implementation of the Montreal Protocol[1] in 1988, the emission of chlorine-containing gases (e.g., chlorofluorocarbons (CFCs) and hydrochlorofluorocarbons (HCFCs)) in the atmosphere has been phasing out. CFCs and HCFCs gases are known to have a strong impact on the depletion of the Earth's ozone layer and high global warming potentials (GWPs).[2,3] Consequently, many efforts have been made to find adequate alternative compounds. The hydrofluorocarbons (HFCs) have emerged as good candidates since they contain no chlorine or bromine atoms in their molecular structure and, therefore, have been assumed to have ozone depletion potential (ODP) near zero.[4,5]

Tetrafluoroethane, CF_3CH_2F, also known as R134a, is a HFC compound widely used as refrigerant in automotive air conditioning, domestic refrigeration systems and aerosol applications.[3,6] The R134a molecule has become one of the best substitutes for chlorine-related compounds due to its low GWP value (1430) and an atmospheric lifetime of 13.8 years.[7] That is consequence of the reactivity with hydroxyl radicals ($OH^•$) found in the troposphere, which leads to smaller atmospheric accumulations. However, despite its advantages, the R134a molecule still contributes to the greenhouse effect and, consequently, to the global warming effect.[8,9] Accordingly, its behavior under irradiation, as in the upper atmosphere, is of great relevance for the impact on the global climate. Knowledge on degradation pathways and energetics is necessary to better understand the photodissociation of the system and to verify if the necessary photon energy is available at low altitudes in the atmosphere.

Apart from its relevance as a refrigerant gas, R134a is also used in radiation particle detectors, especially in resistive plate chambers,[10,11] as a gas insulator[12] and, more recently, as a substrate for environmentally friendly solvents.[13,14] Moreover, in plasma-based technologies, important benefits in different techniques have been shown, such as plasma enhanced

Received: February 13, 2021
Revised: May 4, 2021
Accepted: May 5, 2021
Published: May 17, 2021

chemical vapor deposition,[15] carbon nanostructures[15] and surface functionalization.[16]

The use of R134a in so many applications requires a comprehensive knowledge of the chemical reactivity of this compound under different conditions, especially in the context of atmospheric chemistry and plasma discharge reactions. Consequently, detailed studies on the R134a molecule have been drawing the attention of experimental and theoretical researchers. The photofragmentation dynamics of R134a was studied using threshold photoelectron−photoion coincidence (TPEPICO) spectroscopy.[7,17,18] Additionally, the vibrational spectra and a conformation analysis of R134a were reported by making use of infrared[19] and Raman spectroscopic techniques[19−21] as well as by ab initio calculations.[22]

Recently, the dissociative channels and electronic properties of ionized and excited states of R134a were investigated by computational chemistry.[23] The authors have shown that CF_3^+ and CHF_2^+ are mainly produced by fragmentation of the parent cation by C−C bond cleavage, whereas $CF_3CH_2^+$ is produced by ion-pair formation or direct ionization. The vertical ionization potential was found to be 13.27 eV. The positive and negative ions formed upon electrical corona discharges at atmospheric pressure were also analyzed through atmospheric pressure chemical ionization mass spectrometry (APCI-MS).[3] Furthermore, studies on interactions of the most abundant ions found in the lower and upper atmosphere (O^+, O_2^+, O^-, O_2^-, H_3O^+, among others) with R134a were also performed with the objective deeply study the influence of the R134a in atmospheric chemistry.[8,9]

From atmospheric to plasma-related sciences, the most fundamental processes are related to collisions between electrons, atoms, radicals, and molecules. Such reactions drive the production of ions and radicals that are involved in the leading mechanisms, such as etching, cleaning, or deposition processes, as well as in astrochemical phenomena.[24] Hence, the availability of reliable electron ionization cross sections as a function of the electron energy is crucial to the optimization and development of such mechanisms. Šašić and co-workers[25,26] have obtained and analyzed a set of electron collision cross sections and transport coefficients for the R134a molecule through a standard swarm procedure in bare R134a and when mixed with argon. Also, Urquijo et al.[27] have measured the drift velocities, the longitudinal coefficient, and the effective ionization coefficient of electron in R134a.

Information on electron attachment interactions has been found on several fluoroalkanes,[28−31] but to the best of our knowledge, experimental studies on electron interactions with the R134a have not been yet reported. In the low energy regime (<10 eV), it is essential to guarantee that two main conditions are fulfilled: a high electron energy resolution and a sufficient electron current in the interaction region even at energies near zero eV. Trochoidal electron monochromators (TEMs) have been shown to be a very good choice.[32] These devices are based on the guiding effect that an axial magnetic field has on low energy electrons, which coupled with an orthogonal electrostatic field produces a geometrical separation of the electrons' trajectories, depending on their energies.

In the present work, we report the positive and negative ion formation upon low energy electron interactions with R134a by making use of a TEM coupled with an Orthogonal Reflectron Time-of-Flight Mass Spectrometer (OReToFMS). Ionization efficiency curves for the seven most abundant fragment ions were obtained, for energies between 10 and 40 eV, in order to determine the threshold energies (th) and ionization mass spectra recorded at 70 and 80 eV (not shown). Finally, dissociative channels in gas-phase R134a, leading to negatively charged ion formation by dissociative electron attachment (DEA), were also investigated within an energy range from 0 to 12 eV. The experimental results are supported by quantum chemical calculations.

EXPERIMENTAL SECTION

Materials. 1,1,1,2-Tetrafluoroethane R-134a (≥99.8%) was purchased from Polo Zero (Lisbon, Portugal).

Experimental Setup. The experiments were carried out in a crossed electron-molecule beam apparatus, recently implemented in the CEFITEC laboratory. The setup consists of an electron source and a home-built trochoidal electron monochromator, coupled with an Orthogonal Reflectron Time-of-Flight Mass Spectrometer (OReToFMS) manufactured by KORE Technology Ltd., UK. Figure 1 represents the setup schematically. The TEM consists of three different groups of lenses, M lenses for the monochromator, C lenses for the collision region lenses, and F lenses for the focusing lenses. The set of M lenses comprises eight electrodes, M1−M8. The filament is a tungsten hairpin configuration (Agar Scientific Ldt., UK) mounted as the electrode M1. The M5 and M6 are dispersion electrodes, which apply an electric field transverse to the external magnetic field. This magnetic field, which has an intensity of ∼4 mT, is created by a pair of Helmholtz coils with 70 cm in diameter, outside the vacuum chamber. After the dispersion zone, electrodes M7 and M8, which have holes off center with respect to the M4 electrode hole, are responsible for focusing the electrons through the electrode C1 into the interaction region. The M2−M8 electrodes potentials are floating to the M1 potential, center of filament, which in turn is floating with respect to the interaction region, establishing the adjustable collision energy. Electrodes C2 and C3 are

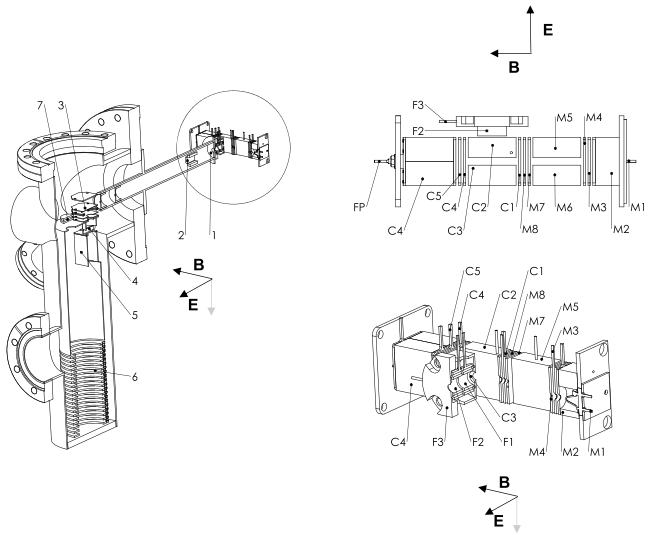

Figure 1. Schematic diagram of trochoidal electron monochromator coupled with orthogonal reflectron time-of-flight mass spectrometer. Left side: assembled TEM with OReToFMS; (1) extract electrode, (2) X and Y ion guide deflectors, (3) ion extraction region; (4) Y deflectors, (5) X deflectors, (6) reflectron, (7) MCP detector. Right side: zoom of TEM showing the labeling of the electrodes where FP = Faraday plate.

https://doi.org/10.1021/jasms.1c00057
J. Am. Soc. Mass Spectrom. 2021, 32, 1459−1468

responsible for applying a small ion extraction field, ~1 V/cm. The C4 and C5 electrodes are responsible for focusing the electrons into a Faraday plate. The C potentials are all set with respect to a fixed potential of ±4 V (for positive or negative mode), either above or below the ground, establishing the optimal kinetic energy positive or negative ions have while entering the orthogonal extraction region of the OReToFMS. Three focusing electrodes, F1, F2, and F3, as well as a set of deflecting electrodes guide the ions from the monochromator to toward the OReToFMS.

Inside the OReToFMS, the extraction region is composed of two circular electrodes placed 245 mm from the entrance of the ion guide. These electrodes produced a pulsed transverse field with respect to the incoming ion beam. The pulses have a frequency of 80 kHz, ±400 V (for positive and negative mode) in amplitude and up to 3 μs pulse width. After being pulsed, the ions can be deflected in two dimensions to optimize their trajectory through the field free flight tube and into the reflectron zone. The reflectron is composed of 24 circular electrodes. After reflection, the ions reach a microchannel plate (MCP) detector; the resulting signal is preamplified and then fed to the data acquisition system. The electron energy can be ramped, by ramping the M electrodes block with respect to the C electrode block, using a National Instruments acquisition board PCIe-6321.

The TEM optimization was first simulated in SIMION[33] software. According to the simulations, an electron energy resolution better than 100 meV should be possible, as well as an ion extraction efficiency for both positive and negative ions above 90%.

Experimentally, with a current applied to the filament of about 2.3 A, an emission current of 100 μA was measured in the electrode M2. The measured current in the Faraday plate for ~0 eV electron energy was ~10 nA and for 70 eV electron energy was ~100 nA. The energy for the positive ions was calibrated by using the well-known Ar^+ threshold energy 15.763 eV, determined by Weitzel et al.[34] through ZEKE-PEPICO (zero kinetic energy photoelectrons photoions coincidence). For negative ions, the energy resolution was determined by the well-known 0 eV resonance for SF_6^- from SF_6 and Cl^- formation from CCl_4 at the full width half-maximum (FWHM). The obtained energy resolution was 130 meV at 0 eV electron energy.

The Ar (gas), SF_6 (gas), and CCl_4 (liquid) samples were introduced in the chamber via a side entrance, whereas solid samples are introduced via an effusive molecular target beam which is created in a molecular oven with 1 mm aperture and aimed orthogonally to the electron beam inside the collision region of the monochromator.

The experiments were performed with a CF_3CH_2F pressure of 6×10^{-4}Pa. The base pressure of the chamber is 3×10^{-6} Pa, achieved with a turbomolecular pump, 300 l/s, Pfeiffer Hipace300. The ToF chamber pressure of 1×10^{-6} Pa was reached with an 80 l/s, Pfeiffer Hipace80 turbomolecular pump.

Acquisition Software. The experimental setup is controlled by homemade software, allowing synchronization between the OReToFMS and a National Instruments board, NI PCIe-6321 Multifunction I/O. This software was made in Labview 19.0;[35] it takes advantage of a dynamic-link library (koretdc.dll) provided by KORE Technology Ldt., UK, in order to access the functionality of the OReToFMS. The Labview program also operates the digital-to-analogue converter (DAC) part of the PCIe-6321 that controls the output voltage required to adjust the electron energy. The interface of the software is composed of various input fields allowing the users to define the parameters associated with the desired measurement. These parameters are the electron energy, the initial and final energy range, the energy step between each mass spectrum, the minimum and maximum mass range, the gate time (time per energy step), the number of runs, the initial and final threshold voltages of time-to-digital converter (TDC), and the calibration parameters Cb and t_0 required for the time-mass conversion, according to

$$m = \left(\frac{t - t_0}{Cb}\right)^2$$

where Cb has the units $\mu s/(amu)^{1/2}$ and t_0 μs; amu stands for atomic mass units.

The software generates a cumulative histogram of ion arrival times, during the respective gate time, at a given energy step. Then the DAC increments the output voltage according to the energy step and repeats this process until the last energy level. The measurements are the sum of several runs in order to increase the signal-to-noise ratio. After the measurement, the software saves all mass spectra in binary files and in a text file with the measurement parameters.

Fitting Procedure. Positive ion efficiency curves have been measured for the seven most abundant fragments (>2% of relative intensity) as a function of the incident electron energy. The ionization energy (IE) for $CF_3CH_2F^+$ (m/z 102) and threshold energies (th_e) for CF_3CHF^+ (m/z 101), $CF_3CH_2^+$ (m/z 83), CF_3^+(m/z 69), CF_2CH^+ (m/z 63), CHF_2^+ (m/z 51), and CH_2F^+ (m/z 33) cations were determined. The ionization energy and threshold energies were experimentally determined using a fitting method based on the well-known Wannier law.[36] The ionization energy and threshold energies were determined according to the function

$$f(e)\begin{cases} f(e) = b; & \text{if } e < \mathrm{IE}(\mathrm{th}_e) \\ f(e) = b + a(e - \mathrm{IE})^d; & \text{if } e \geq \mathrm{IE}(\mathrm{th}_e) \end{cases}$$

where e represents the electron energy and b, a, d, and IE (th_e) are variable fitting parameters. The fittings were performed taking into account three different measurements, in which the corresponding threshold energies relate to the averaged signal. Uncertainties have been determined by accounting for the maximum mean deviation and the statistical uncertainty of the fitting. The statistical uncertainty was calculated by the square root of the covariance matrix diagonal. The total uncertainty value is given by the square root of the sum of the uncertainty values squared.

Theoretical Details. In order to investigate the neutral, positively and negatively charged molecular products, gas-phase calculations on both bound state and scattering techniques were performed. The optimized geometry of neutral CF_3CH_2F was obtained at the MP2/aug-cc-pVDZ level of theory, and a detailed frequency analysis at room temperature of the neutral ground state can be found in the Supporting Information (Table S1). Calculations based on density functional theory (DFT) are also shown for comparison. Symmetry aspects were explored, since the R134a ground state belongs to the Cs point group. Multiconfigurational CASSCF/CASPT2 methods, as implemented in OpenMolcas software,[37] were used for excited state

https://doi.org/10.1021/jasms.1c00057
J. Am. Soc. Mass Spectrom. 2021, 32, 1459−1468

predictions. For these calculations, we used the ANO-L basis set with the contraction scheme [4s3p1d] for fluorine and carbon atoms and [2s1p] for the hydrogen atoms.[38−40] The multistate (MS-CASPT2) diagonalization technique was employed to estimate the excitation energies. The active space comprised 12 electrons in 12 orbitals. In general, the selected orbitals present a nonbonding character, and in some cases, they have hybrid nonbonding/bonding or nonbonding/antibonding characteristics along some specific bonds. For that reason, we have labeled the occupied orbitals *nk*, with k = 1, ..., 6, in decreasing order of energy, while the virtual orbitals are labeled by *nk**, with k = 1, ..., 6, in increasing order of energy. In this order, *n*1 denotes the HOMO and *n*1* the LUMO (see Table 3).

The study of positive ions was separated into two sets of calculations. We first focused on the electron ionization process. The cross sections for ionization out of the individual molecular orbitals, as a function of the collision energy, were estimated using the Binary-Encounter-Bethe (BEB) model, which is known to be accurate for low energy processes—up to tens of eV—and for systems not containing heavy elements.[41] The total ionization cross section (TICS) is taken as a sum over the valence electrons of the target (see Figure 3). The BEB cross section depends on the kinetic energy u and on the binding energy B of the orbital from which the electron is removed, and both properties were calculated with the outer valence Green's function (OVFG) propagator methodology,[42,43] as implemented in the Gaussian09 software.[44] The Hartree−Fock (HF) solution was taken as reference, and the 6-311G(2df,2p) basis set was employed. The six core orbitals of the HF reference were kept frozen in the OVGF calculations. Also, the numbering of the occupied orbitals here follows the label n = 7, ..., 25, in increasing order of energy. In addition, we evaluated the dissociation thresholds for reactions of the type considering all possible fragments A and B produced by single bond breaks, in addition to a few rearrangement channels (see Table 2 and Table S2). The threshold estimates were obtained from the G4(MP2)[45,46] procedure as implemented in Gaussian09. Particularly for the formation of $CF_3CH_2F^+$, the threshold coincides with the first ionization potential (IP1). Also, the geometry optimization and a detailed frequency analysis at room temperature for the cation ground state were addressed at the MP2/aug-cc-pVDZ level of theory. The result is shown in the Figure S4 and may hopefully provide insight into the nuclear relaxation driven by the ionization.

For the negative ion, we first investigated possible bound anion states, finding neither valence-bound nor dipole-bound stable anions for the optimal geometry of the neutral molecule. We then performed fixed-nuclei electron scattering calculations to investigate low energy resonances that could initiate fragmentation processes. For this study, we employed the Schwinger Multichannel[47,48] method implemented with pseudopotentials proposed by Bachelet, Hamann, and Schluter (SMCPP).[49] A detailed theoretical description of the method can be found elsewhere.[50] Finally, the dissociation thresholds were evaluated with the G4(MP2) method for the reactions of type $CF_3CH_2F + e \leftrightarrow CF_3CH_2F^{\#-} \rightarrow A^- + B$. We consider the fragments A and B arising from single bond breaks and also a few rearrangement channels (see Table S3).

RESULTS AND DISCUSSION

Positive Ions. Figure 2 shows the positive mass spectrum recorded at 70 eV incident electron energy with a CF_3CH_2F

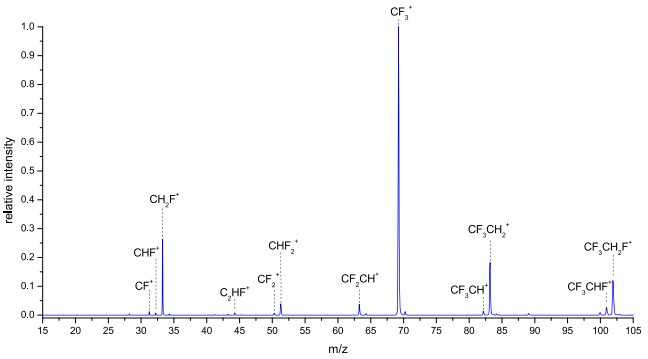

Figure 2. CF_3CH_2F electron ionization mass spectrum recorded at 70 eV incident electron energy. The relative intensities are given in relation to the CF_3^+ peak intensity.

pressure of 9 × 10^{-4} Pa. This energy is well above the ionization threshold of the parent molecule; therefore, many fragmentation pathways are accessible. As far as the authors are aware, no positive mass spectrum has been reported for electron ionization, apart from the NIST chemistry WebBook.[51] Table 1 summarizes the fragments observed upon electron ionization and compares them with photon ionization (PI) study by Morcelle et al.[7] at 40 and 290 eV.

In the present study, 21 cations were observed. CF_3^+ corresponds to the most abundant fragment, in agreement

Table 1. List of Observed Cationic Fragments upon Electron Interactions with the R134a Molecule at 70 eV Electron Energy[a]

cation	*m/z*	EI 70 eV	PI 40 eV	PI 290 eV
$CF_3CH_2F^+$	102	√	√	√
CF_3CHF^+	101	√	×	×
CF_3CF^+	100	√	×	×
$CF_3CH_2^+$	83	√	√	√
$CHCF_3^+$	82	√	×	×
CF_3^+	69	√	√	√
$CF_2CH_2^+$	64	√	×	×
$C_2HF_2^+$	63	√	√	√
CHF_2^+	51	√	√	√
CF_2^+	50	√	×	×
$C_2H_2F^+$	45	√	×	×
C_2HF^+	44	√	×	√
C_2F^+	43	√	×	×
CH_2F^+	33	√	√	√
CHF^+	32	√	×	×
CF^+	31	√	√	√
$C_2H_2^+$	26	√	×	×
C_2H^+	25	√	×	×
C_2^+	24	√	×	√
FH^+	20	√	×	×
F^+	19	√	×	√
C^+	12	×	×	√
H^+	1	×	√	√

[a]The two right columns summarize the photon ionization observations at 40 and 290 eV photon energy described in ref 7, respectively.

https://doi.org/10.1021/jasms.1c00057
J. Am. Soc. Mass Spectrom. 2021, 32, 1459−1468

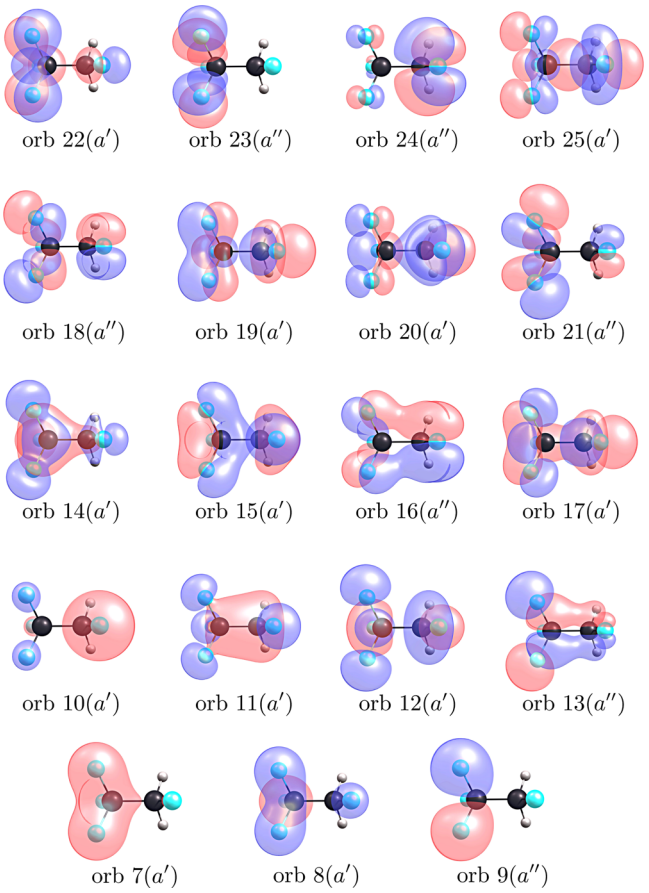

Figure 3. Panel of the 19 molecular orbitals considered for the TICS calculation. The orbitals were obtained at the OVFG/6-311G(2df,2p) level of theory and rendered with the iso value 0.04. The symmetries of the orbitals are also indicated.

with PI studies, but in contrast with the NIST Chemistry WebBook,[51] where CFH_2^+ is indicated as the most abundant cation followed by $CF_3CH_2^+$ and CF_3^+. Moreover, in the present study, the parent cation is formed as one of the six most intense fragments, in contrast with NISH Chemistry WebBook. We found that the signals of the other channels were normalized by the CF_3^+ peak intensity. Out of the 21 observed fragments, only seven intensities were present above 2%, so the 14 remaining fragments can be viewed as minor. The most intense signals were CF_3^+, CH_2F^+, $CF_3CH_2^+$, $CF_3CH_2F^+$, CHF_2^+, CF_2CH^+, and CF_3CHF^+, listed in decreasing order of peak intensities. For those cationic fragments, the proposed reactions can be described as

$$CF_3CH_2F + e \rightarrow CF_3CH_2F^+ + 2e \quad (1)$$

$$CF_3CH_2F + e \rightarrow CF_3CHF^+ + 2e + H^\bullet \quad (2)$$

$$CF_3CH_2F + e \rightarrow CF_3CH_2^+ + 2e + F^\bullet \quad (3)$$

$$CF_3CH_2F + e \rightarrow CF_3^+ + 2e + CH_2F^\bullet \quad (4)$$

$$CF_3CH_2F + e \rightarrow CFH_2^+ + 2e + CF_3^\bullet \quad (5)$$

$$CF_3CH_2F + e \rightarrow CF_2CH^+ + 2e + F_2H^\bullet \quad (6)$$

$$CF_3CH_2F + e \rightarrow CHF_2^+ + 2e + CHF_2^\bullet \quad (7)$$

By increasing the electron energy, the ionization energy has been experimentally obtained and compared with the value obtained using the BEB model. The ionization energy of CF_3CH_2F (reaction 1) was experimentally determined as 13.10 ± 0.17 eV and the first ionization potential estimated at 13.64 eV. The energy dependence ion curve for CF_3CH_2F shows a change in the slope at 14.25 eV that corresponds to the second ionization potential, estimated as 14.27 eV (see Figure S2), corresponding to the removal of an electron from the HOMO +1 orbital. The agreement between the experimentally obtained values and the theoretical ones is good. The BEB total ionization cross section has a peak maximum at 111 eV (see Figur S3).

It is important to note that since BEB predictions of IPs correspond to the absolute values of the OVFG energies of the molecular orbitals, it is not unreasonable to obtain slightly overestimated values. For comparison, an additional vertical IP based on single point calculations at the DFT/B3LYP/aug-cc-pVDZ level was estimated at 13.19 eV, which is in better agreement with the first ionization potential obtained experimentally.

We also surveyed the energy and optimized geometry of the cation ground state. The investigation gives insight on how the nuclear relaxation occurs after the electron-induced ionization. The energy of the optimized cation was calculated at the MP2/aug-cc-pVDZ level, and it was found at 12.31 eV above the neutral ground state. This value can be interpreted as the adiabatic ionization energy of the cation ground state, and the difference between a given IP value and 12.31 eV plays an important role in the nuclear dynamics triggered by the corresponding process. Comparing the cation optimized geometry with the neutral optimized geometry (see Figure S4), we observe a considerable stretching of the C−C bond length (1.52−1.96 Å), indicating that vibronic coupling with the symmetrical C−C stretching vibrational mode may favor a C−C bond break during nuclear dynamics.

Threshold Energies. Reactions 2−7 describe the possible fragmentation pathways for the most six abundant cations. In Table 2, relative intensities are summarized together with experimentally obtained threshold energies (Figure 4) and compared with theoretically estimated values.

The most abundant fragment corresponds to CF_3^+ (m/z 69) (reaction 4), that in turn is associated with the C−C bond break. The experimentally obtained formation threshold was 13.39 ± 0.10 eV, which is above the theoretically estimated

Table 2. List of the Observed Cationic Fragments with Relative Intensities >2%; Experimental Threshold Formation for the Respective Cation and Theoretical Value Estimated at 298.15 K

cation	m/z	rel intensity	experimental threshold (eV)	theoretical threshold (eV)
$CF_3CH_2F^+$	102	0.12	13.10 ± 0.17	13.64[a]/13.19[b]
CF_3CHF^+	101	0.03	14.56 ± 0.17	13.47
$CF_3CH_2^+$	83	0.18	15.51 ± 0.11	13.41/13.70[c]
CF_3^+	69	1	13.39 ± 0.10	12.71
$CHCF_2^+$	63	0.04	16.99 ± 0.25	16.21
CHF_2^+	51	0.04	14.03 ± 0.64	12.43
CH_2F^+	33	0.26	13.36 ± 0.17	12.62

[a]Value obtained with BEB method. [b]Value obtained with DFT/B3LYP/aug-cc-pVDZ method. [c]Value depends on the fluorine atom position (see Table S2).

https://doi.org/10.1021/jasms.1c00057
J. Am. Soc. Mass Spectrom. 2021, 32, 1459−1468

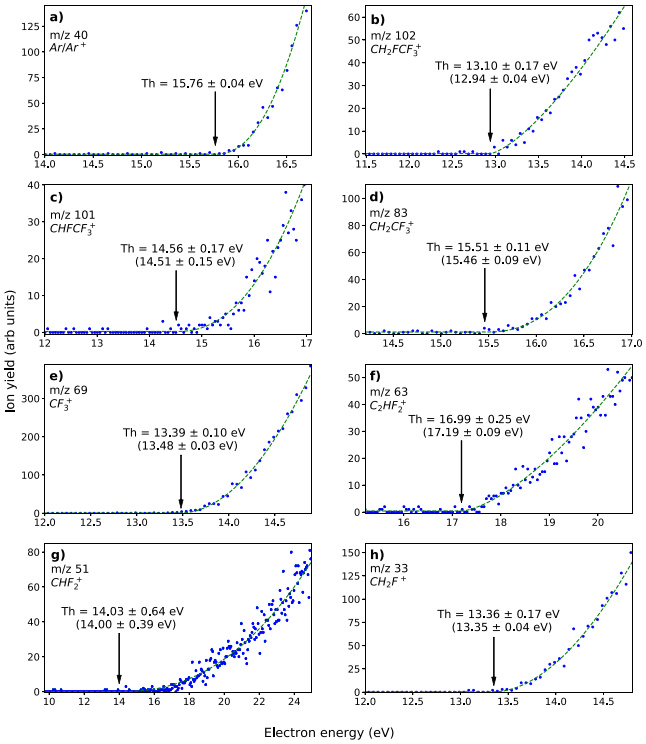

Figure 4. Experimental thresholds for the seven most abundant cations (panels b–h). The blue dots represent the experimental data, and the green dashed line represents the Wannier-type fitting function. The threshold (Th) values are the average of three different measurements, and the values in the brackets correspond to the presented fits, together with their respective statistical uncertainties. The energy scale was calibrated based on the well-known Ar^+ threshold (panel a), measured before and after the R134a molecule measurement.

value of 12.71 eV. The complementary reaction leads to CH_2F^+ (m/z 33) formation (reaction 5) with an average intensity of ~60% being the second most intensely formed fragment. The threshold energy for this pathway was found to be 13.36 ± 0.17 eV, also slightly above the theoretically estimated value of 12.62 eV. At energies between IP1 and IP2 these two complementary reactions involve the electron ejection from orbital 25 (see Figure 4), which has a bonding characteristic along the C–C bond. That is compatible with the nuclear relaxation path triggered by the ionization, thus being consistent with the C–C bond break. For energies above IP2, other mechanisms may take place since other electrons are ejected. However, it is to be expected that orbitals with bonding character along the C–C bond would have a larger influence on both CF_3^+ and CH_2F^+ signals. The third most intense signal is $CF_3CH_2^+$ (m/z 83) following reaction 3 with elimination of a fluorine radical as a neutral counterpart. The experimentally determined threshold was obtained as 15.51 ± 0.11 eV compared with the theoretically estimated values 13.41 or 13.70 eV depending on the fluorine atom position (see Table S2). The experimental threshold indicates the reaction may not occur through the ionization from orbitals 25 and 24, although the corresponding channels would be energetically opened. Instead, 15.51 eV might be assigned to the IP3, estimated as 15.64 eV and corresponding to orbital 23, which is delocalized over the fluorine atoms of the CF_3 group. On the other hand, IP4 (estimated as 16.08 eV) and IP5 (estimated as 16.09 eV) are associated with orbitals 22 and 21, respectively, which also present bonding/nonbonding features on all four fluorine atoms. That said, our understanding of the m/z 83 signal is that the measurements between the experimental threshold (15.51 ± 0.11 eV) and about 16 eV correspond exclusively to the elimination of fluorine atoms 6, 7, and 8—they are equivalent because of symmetry and rotation (see Figure S1)—while from 16 eV up there is competition among fragmentation channels regarding all fluorine atoms. Reaction 7 describes the formation of CHF_2^+ (m/z 51). The threshold energy was found at 14.03 ± 0.64 eV, whereas the estimated theoretical value was predicted as 12.43 eV. The formation of CHF_2^+ occurs via a complex rearrangement reaction path. It involves a C–C bond break, a fluorine donation between groups followed by a hydrogen elimination. Thus, it is not easy to assign the role of a given molecular orbital. Particularly at energies near threshold, the pathway leading to the formation of such cation involves electron removal from the orbital 25 for energetic arguments; however, the signal significantly increases from 15 eV, making it difficult to establish clear conclusions and infer about the energy involved in rearrangement reactions. Reaction 6 leads to the formation of CF_2CH^+ (m/z 63). The theoretical estimated energy was found at 16.21 eV in good agreement with experimentally determined 16.99 ± 0.25 eV. This is another case of a complex reaction, which may involve a fluorine atom elimination from the CF_3 group along with a HF elimination from the CH_2F group or possibly an even more complicated rearrangement. Ionization from orbitals 18 (IP8 = 17.21 eV) and 17 (IP9 = 17.81 eV) are assigned to be the process triggering the formation of a CF_2CH^+ fragment at energies near the threshold. Moreover, the dehydrogenated parent cation CF_3CHF^+ (m/z 101), has not been identified by photoionization studies.[7] The experimentally determined threshold was found to be 14.56 ± 0.17 eV, somewhat above the theoretically predicted value of 13.47 eV.

Minor Fragments. Apart from the parent cation and the most abundant fragments mentioned above, 14 other fragments have been identified with relative intensities below 2%. Due to the low intensities, the threshold determination is very inaccurate; hence, they are not discussed here. The loss of two H atoms was observed for the formation of CF_3CF^+ (m/z 100). This fragment has not been identified by photoionization studies.[7] The theoretically estimated threshold energy value was found to be 14.02 eV. CF_3CH^+ (m/z 82), $CF_2CH_2^+$ (m/z 64), and CF_2^+ (m/z 50) fragment cations were also observed, and their respective energy thresholds were determined as 10.98, 15.57, and 13.05 eV, respectively. These three fragments were not reported in PI studies by Morcelle et al.,[7] not were $CFCH_2^+$ (m/z 45), CFC^+ (m/z 43), CHF^+ (m/z 32), $C_2H_2^+$ (m/z 26), C_2H^+ (m/z 25), and HF^+ (m/z 20). Finally, four additional fragments were identified as $CFCH^+$ (m/z 44), C_2^+ (m/z 24), and F^+ (m/z 19), reported by Morcelle et al.[7] at 290 eV impact photon energy, and CF^+ (m/z 31), reported by Morcelle et al.[7] at 40 and 290 eV impact photon energy. All estimated thresholds are summarized in Table S3. Although the experimental determination of the thresholds was inaccurate, no formation of fragments below the theoretical threshold was observed.

Negative Ions. For electron energies below 15 eV, molecules may attach an electron of specific kinetic energy to form temporary negative ions (TNIs), $[MX]^{\#-}$, that can have typical lifetimes ranging from 10^{-15} to $>10^{-12}$ s.[24,52] Subsequently, a TNI decays by either spontaneous electron

https://doi.org/10.1021/jasms.1c00057
J. Am. Soc. Mass Spectrom. 2021, 32, 1459–1468

emission (autodetachment), which may leave the neutral molecule in an excited state, or by dissociation into a negatively charged fragment, $[M-X]^-$, and one (or more) neutrals:

$$MX + e^- \leftrightarrow [MX]^{\#-} \rightarrow [M - X]^- + X \quad (8)$$

This fragmentation process is known as dissociative electron attachment (DEA).

In order to identify the short-lived TNI states formed by electron attachment to the R134a molecule, we have investigated electron elastic scattering from R134a using the SMCPP method. Since the neutral species has a high-lying threshold for electronic excitation around 9.31 eV (see Table 3 containing CASPT2 results), the scattering calculations only consider the elastic channel. This procedure is adequate to investigate the formation of shape resonances at subexcitation energies, although not for core-excited TNIs. The elastic ICS for both A′ and A″ symmetry components are shown in Figure 5. The more accurate SEP results indicate three shape

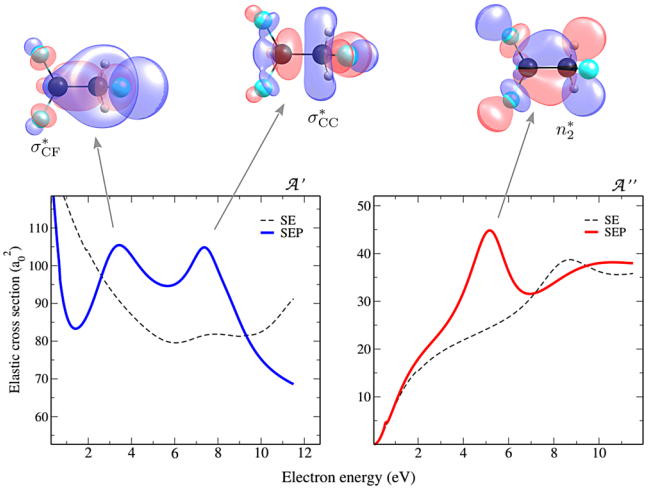

Figure 5. Electronic scattering cross section for the elastic channel, decomposed in A′ (left panel) and A″ (right panel) symmetries. The thick lines stand for the results in the SEP approximation, while the dashed lines stand for that in the SE approximation. The σCF*, σCC*, and n2* virtual orbitals are also shown.

resonances, namely two resonances σ_{CF}* and σ_{CC}* at positions (widths) 3.87 (0.87) and 7.48 (0.40) eV in the A′ component and an n_2* shape resonance at 5.32 (0.39) eV in the A″ component. These resonances have been labeled according to the character of the neutral virtual orbitals involved in the electron attachment processes (see Figure 5).

Using the novel assembly described above, we have investigated experimentally the DEA to the R134a molecule in the energy regime from about 0 up to 12 eV. Considering the detection limit of the ToF mass spectrometer and the minimum anion lifetime allowing it to reach the detector ($\sim 10^{-6}$ s), we have observed one single fragment anion $C_2F_3^-$ (m/z 81) arising from the following DEA reaction:

$$CF_3CH_2F + e^- \leftrightarrow CF_3CH_2F^{\#-} \rightarrow C_2F_3^- + H_2F^\bullet \quad (9)$$

Figure 6 shows the ion yield of the fragment $C_2F_3^-$ (m/z 81) together with a cumulative peak fit obtained following multiple fits of the observed structures.

In addition to a resonant feature peaking at 9.2 eV, two less intense shoulders at 10.3 and 11.2 eV are also observed. By

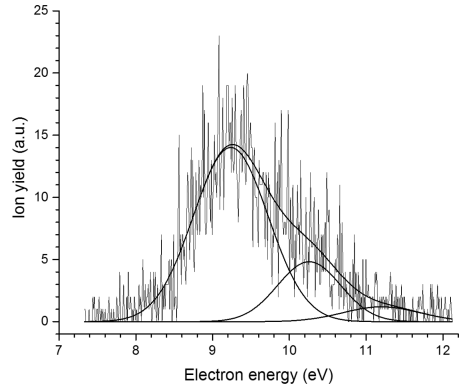

Figure 6. Ion yield of the fragment anion $C_2F_3^-$ (m/z 81) formed by dissociative electron attachment (DEA) to R134a. The solid line represents the cumulative fitting of multiple Gaussian functions.

employing the method proposed by Meißner et al.,[53] the formation of $C_2F_3^-$ via DEA to R134a has been determined to have an experimental onset of 8.3 eV. This result suggests that the three shape resonances σ_{CF}*, σ_{CC}*, and n_2* are not precursors of the reaction, as the experimental onset lies energetically above their calculated positions. Consequently, given that DEA to R134a appears to take place between 9.0 and 12 eV electron energy, the incoming electron can be captured into a virtual orbital following an electronic excitation, leading to the formation of a core-excited resonance. CASPT2 excitation energies of the singlet and triplet states lying below the first ionization potential are shown in Table 3. The excited triplet states T_n (n = 1−5) as

Table 3. Vertical Electronic States for Neutral R134a Obtained at the CASSCF/CASPT2 Level of Theory[a]

electronic state (neutral)	energy (eV)
S0	0
T1 ($n_1 \rightarrow n_1$*)	9.31
T2 ($n_2 \rightarrow n_1$*)	9.54
S1 ($n_2 \rightarrow n_1$*)	10.21
S2 ($n_1 \rightarrow n_2$*)	10.30
T3 ($n_2 \rightarrow n_2$*)	10.37
T4 ($n_2 \rightarrow n_2$*)	11.01
S3 ($n_2 \rightarrow n_6$*)	11.30
S4 ($n_1 \rightarrow n_6$*)	11.31
T5 ($n_4 \rightarrow n_1$*)	12.00
T6 ($n_6 \rightarrow n_1$*)	12.78
T7 ($n_1 \rightarrow n_2$*)/($n_4 \rightarrow n_2$*)	13.21
S5 ($n_6 \rightarrow n_1$*)	13.41
S6 ($n_6 \rightarrow n_6$*)	13.81
T8 ($n_6 \rightarrow n_2$*)	13.96

[a]S and T stand for singlet and triplet states, respectively.

well as the singlet states S_n (n = 1−4) lie within the energy range from 9.0 to 12 eV and can mediate the formation of core-excited resonances that may in turn dissociate into $C_2F_3^-$, along with a neutral counterpart $H_2F^\bullet$. The G4(MP2) prediction for the dissociation threshold of reaction 7) was 7.41 eV, which is consistent with the experimental onset.

It is also important to point out that no other anionic fragments were observed. That indicates that not only do the described shape resonances play no role on the $C_2F_3^-$ DEA channel but they do not mediate dissociations on the R134a

https://doi.org/10.1021/jasms.1c00057
J. Am. Soc. Mass Spectrom. 2021, 32, 1459−1468

molecule considering all studied channels. That can be justified based on the broad structures of the TNIs signatures. The widths of the states correspond to lifetimes of 0.8 fs, 1.7 and 1.6 fs, respectively, which are small compared to typical timescales of nuclear relaxations. Even though we are dealing with a fixed nuclei approximation for the lifetimes, the values are short enough to suggest that the formation of such TNIs are essentially followed by autodetachment.

CONCLUSIONS

In the present study, we have explored and described electron ionization and dissociative electron attachment of the R134a refrigerant gas by using a high-resolution trochoidal electron monochromator coupled with an orthogonal reflectron time-of-flight mass spectrometer, as well as by a comprehensive quantum chemical approach. A comprehensive knowledge of the photophysics of this system is required to understand the potential photochemical degradation pathways. From the electron ionization study, it was possible to determine the ionization energy of R134a, found at 13.10 ± 0.17 eV, and the second ionization potential found at 14.25 eV, in good agreement with BEB and MP theoretical calculations. The appearance energies for the six most abundant fragment cations, have been experimentally determined. The results were successfully supported by theoretical calculations, which also contributed to the characterization of the fragmentation pathways as well as important aspects of the electronic structures involved in the processes. We have also shown experimentally that DEA to R134a leads to the formation of a single anion fragment ($C_2F_3^-$). Based on our electron scattering calculations, as well as on our estimates of the excited states of the neutral R134a, we conclude that $C_2F_3^-$ formation occurs via formation of at least three core-excited resonances lying between 9 and 12 eV. A detailed characterization of the energetics and lifetimes of the shape resonances supported by the R134a molecule is presented.

ASSOCIATED CONTENT

Supporting Information

The Supporting Information is available free of charge at https://pubs.acs.org/doi/10.1021/jasms.1c00057.

Theoretical methods, computational procedures, auxiliary results, additional orbital panels, and a complete table of dissociation thresholds (PDF)

AUTHOR INFORMATION

Corresponding Authors

Filipe Ferreira da Silva − *CEFITEC, Departamento de Física, Faculdade de Ciências e Tecnologia, Universidade NOVA de Lisboa, 2829-516 Caparica, Portugal;* orcid.org/0000-0002-2182-2965; Email: f.ferreiradasilva@fct.unl.pt

Lucas M. Cornetta − *Instituto de Física Gleb Wataghin da Universidade Estadual de Campinas, 13083-859 Campinas, Brazil*; Email: lucascor@unicamp.br

Authors

João Pereira-da-Silva − *CEFITEC, Departamento de Física, Faculdade de Ciências e Tecnologia, Universidade NOVA de Lisboa, 2829-516 Caparica, Portugal*

Rodrigo Rodrigues − *CEFITEC, Departamento de Física, Faculdade de Ciências e Tecnologia, Universidade NOVA de Lisboa, 2829-516 Caparica, Portugal*

João Ramos − *CEFITEC, Departamento de Física, Faculdade de Ciências e Tecnologia, Universidade NOVA de Lisboa, 2829-516 Caparica, Portugal*

Carlos Brígido − *CEFITEC, Departamento de Física, Faculdade de Ciências e Tecnologia, Universidade NOVA de Lisboa, 2829-516 Caparica, Portugal*

Alexandru Botnari − *CEFITEC, Departamento de Física, Faculdade de Ciências e Tecnologia, Universidade NOVA de Lisboa, 2829-516 Caparica, Portugal*

Miguel Silvestre − *CEFITEC, Departamento de Física, Faculdade de Ciências e Tecnologia, Universidade NOVA de Lisboa, 2829-516 Caparica, Portugal*

João Ameixa − *CEFITEC, Departamento de Física, Faculdade de Ciências e Tecnologia, Universidade NOVA de Lisboa, 2829-516 Caparica, Portugal;* orcid.org/0000-0001-8648-9924

Mónica Mendes − *CEFITEC, Departamento de Física, Faculdade de Ciências e Tecnologia, Universidade NOVA de Lisboa, 2829-516 Caparica, Portugal*

Fábio Zappa − *Departamento de Física-ICE, Universidade Federal de Juiz de Fora, 36036-900 Juiz de Fora, MG, Brazil*

Stephen J. Mullock − *Kore Technology Ltd., Cambridge CB4 4WF, U.K.*

João M. M. Araújo − *LAQV, REQUIMTE, Departamento de Química, Faculdade de Ciências e Tecnologia, Universidade NOVA de Lisboa, 2829-516 Caparica, Portugal;* orcid.org/0000-0002-8648-7539

Márcio T. do N. Varella − *Instituto de Física, Universidade de São Paulo, 05508-090 São Paulo, Brazil;* orcid.org/0000-0002-5812-0342

Complete contact information is available at: https://pubs.acs.org/10.1021/jasms.1c00057

Author Contributions

The manuscript was written through contributions of all authors. J.P.d.S., R.R., J.R., and C.B. were involved in setup assembly and optimization, together with A.B., M.S., and J.A. for trochoidal monochromator electronics development and assembling; J.P.d.S., R.R., J.R., and F.F.d.S. performed data acquisition and analysis together with J.M.M.A.; J.P.d.S., M.M., and F.F.d.S. prepared the first draft of the manuscript; L.M.C. and M.T.d.N.V. performed quantum chemical calculations and prepared the draft; F.Z. and S.J.M. performed technical and optimization contributions; M.M., F.Z., L.M.C., M.T.d.N.V., S.J.M., J.M.M.A., and F.F.d.S. prepared the final revision before submission. All authors have given approval to the final version of the manuscript.

Notes

The authors declare no competing financial interest.

ACKNOWLEDGMENTS

J.P.d.S. and J.A. acknowledge the Portuguese National Funding Agency FCT-MCTES through grants PD/BD/142768/2018 and PD/BD/114447/2016 respectively. F.F.d.S. and M.M. acknowledge the research grant PTDC/FIS-AQM/31215/2017. J.M.M.A. also acknowledges FCT-MCTES project PTDC/EQU-EQU/29737/2017. This work was also supported by the Associate Laboratory for Green Chemistry-LAQV, which is financed by national funds from FCT/MCTES (UIDB/50006/2020 and UIDP/50006/2020) as well as support from the Radiation Biology and Biophysics Doctoral Training Programme (RaBBiT, PD/00193/2012), UID/

Multi/04378/2019(UCIBIO), and UID/FIS/00068/2020 (CEFITEC). M.T.d.N.V. acknowledges the Brazilian National Council for Scientific and Technological Development (CNPq, grant no. 304571/2018-0), L.M.C. acknowledges financial support from the São Paulo Research Foundation (FAPESP). The authors also acknowledge the technician Afonso Moutinho for technical support during setup assembly.

REFERENCES

(1) *Montreal Protocol on Substances That Deplete the Ozone Layer Montreal* **1989**, *Vol. C.*

(2) Simmonds, P.; O'Doherty, S.; Huang, J.; Prinn, R.; Ryall, D.; Nickless, G.; Cunnold, D. Calculated Trends and the Atmospheric Abundance of 1,1,1,2-Tetrafluoroethane, 1,1-Dichloro-1-Fluoroethane, and 1-Chloro-1,1-Difluoroethane Using Automated in-Situ Gas Chromatography-Mass Spectrometry Measurements Recorded at Mace Head, Ireland, from Octod. *J. Geophys. Research* **1998**, *103*, 16029−16037.

(3) Marotta, E.; Paradisi, C.; Scorrano, G. An Atmospheric Pressure Chemical Ionization Study of the Positive and Negative Ion Chemistry of the Hydrofluorocarbons 1,1-Difluoroethane (HFC-152a) and 1,1,1,2-Tetrafluoroethane (HFC-134a) and of Perfluoro-n-Hexane (FC-72) in Air Plasma at Atmospheric Pr. *J. Mass Spectrom.* **2004**, *39*, 791−801.

(4) Ravishankara, A. R.; Turnipseed, A. A.; Jensen, N. R.; Barone, S.; Mills, M.; Howard, C. J.; Solomon, S. Do Hydrofluorocarbons Destroy Stratospheric Ozone? *Science* **1994**, *263*, 71−75.

(5) Montzka, S. A.; Myers, R. C.; Butler, J. H.; Elkins, J. W.; Lock, L. T.; Clarke, A. D.; Goldstein, A. H. Observations of HFC-134a in the Remote Troposphere. *Geophys. Res. Lett.* **1996**, *23*, 169−172.

(6) Aziz, A.; Izzudin, I.; Mainil, A. K. Performance Comparison of a Refrigerator System Using R134a and Hydrocarbon Refrigerant (HCR134a) with Different Expansion Devices. *IOP Conf. Ser.: Mater. Sci. Eng.* **2017**, *237*, 012008.

(7) Morcelle, V.; Medina, A.; Ribeiro, L. C.; Prazeres, I.; Marinho, R. R. T.; Arruda, M. S.; Mendes, L. A. V.; Santos, M. J.; Tenório, B. N. C.; Rocha, A. B.; Santos, A. C. F. Fragmentation of Valence and Carbon Core Excited and Ionized CH 2 FCF 3 Molecule. *J. Phys. Chem. A* **2018**, *122*, 9755−9760.

(8) Morris, R. A.; Viggiano, A. A.; Arnold, S. T.; Paulson, J. F.; Liebman, J. F. Reactions of Atmospheric Ions with Selected Hydrofluorocarbons. *J. Phys. Chem.* **1995**, *99*, 5992−5999.

(9) Morris, R. A.; Viggiano, A. A.; Arnold, S. T.; Paulson, J. F. Chemistry of Atmospheric Ions Reacting with Fully Fluorinated Compounds. *Int. J. Mass Spectrom. Ion Processes* **1995**, *150*, 287−298.

(10) Riegler, W.; Lippmann, C.; Veenhof, R. Detector Physics and Simulation of Resistive Plate Chambers. *Nucl. Instrum. Methods Phys. Res., Sect. A* **2003**, *500*, 144−162.

(11) Abbrescia, M.; Colaleo, A.; Guida, R.; Iaselli, G.; Loddo, F.; Maggi, M.; Marangelli, B.; Natali, S.; Nuzzo, S.; Pugliese, G.; Ranieri, A.; Romano, F.; Roselli, G.; Trentadue, R.; Tupputi, S.; Benussi, L.; Bertrani, M.; Caponero, M.; Colonna, D.; Donisi, D.; Fabbri, F.; Felli, F.; Giardoni, M.; Pallotta, M.; Paolozzi, A.; Passamonti, M.; Pucci, C.; Saviano, G.; Polese, G.; Fabozzi, F.; Cimmino, A.; Paolucci, P.; Piccolo, D.; Noli, P.; Belli, G.; Grelli, A.; Necchi, M.; Ratti, S.; Riccardi, C.; Torre, P.; Vitulo, P.; Genchev, V.; Iaydjiev, P.; Stoykova, S.; Sultanov, G.; Trayanov, R.; Dimitrov, A.; Litov, L.; Pavlov, B.; Petkov, P. The Gas Monitoring System for the Resistive Plate Chamber Detector of the CMS Experiment at LHC. *Nucl. Phys. B, Proc. Suppl.* **2008**, *177−178*, 293−296.

(12) McAllister, I. W. Journal of Physics D: Applied Physics. *J. Phys. D: Appl. Phys.* **1989**, *22*, 1783−1784.

(13) Sosa, J. E.; Ribeiro, R. P. P. L.; Castro, P. J.; Mota, J. P. B.; Araújo, J. M. M.; Pereiro, A. B. Absorption of Fluorinated Greenhouse Gases Using Fluorinated Ionic Liquids. *Ind. Eng. Chem. Res.* **2019**, *58*, 20769−20778.

(14) Castro, P. J.; Redondo, A. E.; Sosa, J. E.; Zakrzewska, M. E.; Nunes, A. V. M.; Araújo, J. M. M.; Pereiro, A. B. Absorption of Fluorinated Greenhouse Gases in Deep Eutectic Solvents. *Ind. Eng. Chem. Res.* **2020**, *59*, 13246−13259.

(15) Vizireanu, S.; Ionita, M. D.; Dinescu, G.; Enculescu, I.; Baibarac, M.; Baltog, I. Post-Synthesis Carbon Nanowalls Transformation under Hydrogen, Oxygen, Nitrogen, Tetrafluoroethane and Sulfur Hexafluoride Plasma Treatments. *Plasma Processes Polym.* **2012**, *9*, 363−370.

(16) Guruvenket, S.; Iyer, G. R. S.; Shestakova, L.; Morgen, P.; Larsen, N. B.; Mohan Rao, G. Fluorination of Polymethylmethaacrylate with Tetrafluoroethane Using DC Glow Discharge Plasma. *Appl. Surf. Sci.* **2008**, *254*, 5722−5726.

(17) Zhou, W.; Seccombe, D. P.; Tuckett, R. P.; Thomas, M. K. Fragmentation of Valence Electronic States of CHF2CF3+ Studied by Threshold Photoelectron-Photoion Coincidence (TPEPICO) Techniques in the Photon Energy Range 12−25 EV. *Chem. Phys.* **2002**, *283*, 419−431.

(18) Zhou, W.; Seccombe, D. P.; Tuckett, R. P. Fragmentation of Valence Electronic States of CF3-CH2F+ and CHF2-CHF2+ in the Range 12−25 EV. *Phys. Chem. Chem. Phys.* **2002**, *4*, 4623−4633.

(19) Craig, N. C.; Chuang, J. I.; Nwofor, C. C.; Oertel, C. M. Synthesis and Vibrational Spectroscopy of 1,1,2,2-Tetrafluoroethane and Its13C2 and D2 Isotopomers. *J. Phys. Chem. A* **2000**, *104*, 10092−10103.

(20) Craig, N. C.; Oertel, C. M.; Oertel, D. C.; Lock, M. Complete Structure of Anti-1,1,2,2-Tetrafluoroethane by High-Resolution Infrared Spectroscopy. *J. Phys. Chem. A* **2001**, *105*, 6008−6019.

(21) Kalasinsky, V. F.; Anjaria, H. V.; Little, T. S. Vibrational Spectra and Conformations of 1,1,2-Trifluoroethane and 1,1,2,2-Tetrafluoroethane. *J. Phys. Chem.* **1982**, *86*, 1351−1357.

(22) Papasavva, S.; Illinger, K. H.; Kenny, J. E. Ab Initio Calculations on Fluoroethanes: Geometries, Dipole Moments, Vibrational Frequencies, and Infrared Intensities. *J. Phys. Chem.* **1996**, *100*, 10100−10110.

(23) Hayashi, T.; Ishikawa, K.; Sekine, M.; Hori, M. Dissociative Properties of 1,1,1,2-Tetrafluoroethane Obtained by Computational Chemistry. *Jpn. J. Appl. Phys.* **2018**, *57*, 4−7.

(24) Christophorou, L. G.; McCorkle, D. L.; Christodoulides, A. A. Electron Attachment Processes. In *Electron-Molecule interactions and their applications Vol1*; Academic Press, Inc.: Orlando, FL, 1984.

(25) Šašić, O.; Dupljanin, S.; Urquijo, J. De; Petrović, Z. L. Scattering Cross Sections for Electrons in C2 H 2F4 and Its Mixtures with Ar from Measured Transport Coefficients. *J. Phys. D: Appl. Phys.* **2013**, *46*, 325201.

(26) Šašić, O.; De Urquijo, J.; Juárez, A. M.; Dupljanin, S.; Jovanović, J.; Hernández-Ávila, J. L.; Basurto, E.; Petrović, Z. L. Measurements and Analysis of Electron Transport Coefficients Obtained by a Pulsed Townsend Technique. *Plasma Sources Sci. Technol.* **2010**, *19*, 034003.

(27) De Urquijo, J.; Juárez, A. M.; Basurto, E.; Hernández-Ávila, J. L. Electron Swarm Coefficients in 1,1,1,2 Tetrafluoroethane (R134a) and Its Mixtures with Ar. *Eur. Phys. J. D* **2009**, *51*, 241−246.

(28) Christophorou, L. G.; Olthoff, J. K. Electron Interactions with Plasma Processing Gase: An Update for CF4, CHF3, C2F6, and C3F8. *J. Phys. Chem. Ref. Data* **1999**, *28*, 967−982.

(29) Torres, I.; Martínez, R.; Castaño, F. Electron-Impact Dissociative Ionization of the CH3F Molecule. *J. Phys. B: At., Mol. Opt. Phys.* **2002**, *35*, 4113.

(30) Torres, I.; Martínez, R.; Sánchez Rayo, M. N.; Castaño, F. Journal of Physics B: Atomic, Molecular and Optical Physics Related Content Electron Impact Dissociative Ionization of the CH 2 F 2 Molecule: Cross Sections, Appearance Potentials, Nascent Kinetic Energy Distributions and Dissociation Pathways Electr. *J. Phys. B: At., Mol. Opt. Phys.* **2000**, *33*, 3615.

(31) Motlagh, S.; Moore, J. H. Cross Sections for Radicals from Electron Impact on Methane and Fluoroalkanes. *J. Chem. Phys.* **1998**, *109*, 432−438.

(32) Grill, V.; Drexel, H.; Sailer, W.; Lezius, M.; Märk, T. D. Operating Principle of an Electron Monochromator in an Axial Magnetic Field. *J. Mass Spectrom.* **2001**, *36*, 151−158.

https://doi.org/10.1021/jasms.1c00057
J. Am. Soc. Mass Spectrom. 2021, 32, 1459−1468

(33) *SIMION*; Scientific Instrument Services, Inc.: Ringoes, NJ.
(34) Weitzel, K. M.; Mähnert, J.; Penno, M. ZEKE-PEPICO Investigations of Dissociation Energies in Ionic Reactions. *Chem. Phys. Lett.* **1994**, *224*, 371−380.
(35) Bitter, R.; Mohiuddin, T.; Nawrocki, M. *LabVIEW: Advanced Programming Techniques*; CRC Press, 2006.
(36) Wannier, G. H. The Threshold Law for Single Ionization of Atoms or Ions by Electrons. *Phys. Rev.* **1953**, *90*, 817−825.
(37) Fdez. Galván, I.; Vacher, M.; Alavi, A.; Angeli, C.; Aquilante, F.; Autschbach, J.; J. Bao, J.; I. Bokarev, S.; A. Bogdanov, N.; K. Carlson, R.; F. Chibotaru, L.; Lindh, R.; Fdez. Galván, I.; Vacher, M.; Alavi, A.; Angeli, C.; Aquilante, F.; Autschbach, J.; J. Bao, J.; I. Bokarev, S.; A. Bogdanov, N.; K. Carlson, R.; F. Chibotaru, L.; Creutzberg, J.; Dattani, N.; G. Delcey, M.; S. Dong, S.; Dreuw, A.; Freitag, L.; Manuel Frutos, L.; Gagliardi, L.; Gendron, F.; Giussani, A.; González, L.; Grell, G.; Guo, M.; E. Hoyer, C.; Johansson, M.; Keller, S.; Knecht, S.; Kovačević, G.; Källman, E.; Li Manni, G.; Lundberg, M.; Ma, Y.; Mai, S.; Pedro Malhado, J.; Åke Malmqvist, P.; Marquetand, P.; A. Mewes, S.; Norell, J.; Olivucci, M.; Oppel, M.; Manh Phung, Q.; Pierloot, K.; Plasser, F.; Reiher, M.; M. Sand, A.; Schapiro, I.; Sharma, P.; J. Stein, C.; Kragh Sørensen, L.; G. Truhlar, D.; Ugandi, M.; Ungur, L.; Valentini, A.; Vancoillie, S.; Veryazov, V.; Weser, O.; A. Wesołowski, T.; Widmark, P.; Wouters, S.; Zech, A.; Patrick Zobel, J.; Lindh, R. OpenMolcas: From Source Code to Insight. *J. Chem. Theory Comput.* **2019**, *15*, 5925−5964.
(38) Pou-AméRigo, R.; Merchán, M.; Ortí, E. Theoretical Study of the Electronic Spectrum of P-Benzoquinone. *J. Chem. Phys.* **1999**, *110*, 9536−9546.
(39) Pou-AméRigo, R.; Serrano-Andrés, L.; Merchán, M.; Ortí, E.; Forsberg, N. A Theoretical Determination of the Low-Lying Electronic States of the p-Benzosemiquinone Radical Anion. *J. Am. Chem. Soc.* **2000**, *122*, 6067−6077.
(40) Widmark, P.-O.; Malmqvist, P.-Å.; Roos, B. O. Density Matrix Averaged Atomic Natural Orbital (ANO) Basis Sets for Correlated Molecular Wave Functions. *Theor. Chim. Acta* **1990**, *77*, 291−306.
(41) Scott, G. E.; Irikura, K. K. Performance of Binary-Encounter-Bethe (BEB) Theory for Electron-Impact Ionization Cross Sections of Molecules Containing Heavy Elements (Z > 10). *Surf. Interface Anal.* **2005**, *37*, 973−977.
(42) Ortiz, J. V. Electron Binding Energies of Anionic Alkali Metal Atoms from Partial Fourth Order Electron Propagator Theory Calculations. *J. Chem. Phys.* **1988**, *89*, 6348−6352.
(43) von Niessen, W.; Schirmer, J.; Cederbaum, L. S. Computational Methods for the One-Particle Green's Function. *Comput. Phys. Rep.* **1984**, *1*, 57−125.
(44) Frisch, M. J.; Trucks, G. W.; Schlegel, H. B.; Scuseria, G. E.; Robb, M. A.; Cheeseman, J. R.; Scalmani, G.; Barone, V.; Petersson, G. A.; Nakatsuji, H.; Li, X.; Caricato, M.; Marenich, A.; Bloino, J.; Janesko, B. G.; Gomperts, R.; Mennucci, B.; Hratchian, H. P.; Ortiz, J. V.; Izmaylov, A. F.; Sonnenberg, J. L.; Williams-Young, D.; Ding, F.; Lipparini, F.; Egidi, F.; Goings, J.; Peng, B.; Petrone, A.; Henderson, T.; Ranasinghe, D.; Zakrzewski, V. G.; Gao, J.; Rega, N.; Zheng, G.; Liang, W.; Hada, M.; Ehara, M.; Toyota, K.; Fukuda, R.; Hasegawa, J.; Ishida, M.; Nakajima, T.; Honda, Y.; Kitao, O.; Nakai, H.; Vreven, T.; Throssell, K.; Montgomery, J. A., Jr.; Peralta, J. E.; Ogliaro, F.; Bearpark, M.; Heyd, J. J.; Brothers, E.; Kudin, K. N.; Staroverov, V. N.; Keith, T.; Kobayashi, R.; Normand, J.; Raghavachari, K.; Rendell, A.; Burant, J. C.; Iyengar, S. S.; Tomasi, J.; Cossi, M.; Millam, J. M.; Klene, M.; Adamo, C.; Cammi, R.; Ochterski, J. W.; Martin, R. L.; Morokuma, K.; Farkas, O.; Foresman, J. B.; Fox, D. J. *Gaussian 09*, Revision A.02; Gaussian, Inc.: Wallingford, CT, 2016.
(45) Curtiss, L. A.; Redfern, P. C.; Raghavachari, K. Gaussian-4 theory. *J. Chem. Phys.* **2007**, *126*, 084108.
(46) Curtiss, L. A.; Redfern, P. C.; Raghavachari, K. Gaussian-4 theory using reduced order perturbation theory. *J. Chem. Phys.* **2007**, *127*, 124105.
(47) Takatsuka, K.; McKoy, V. Extension of the Schwinger Variational Principle beyond the Static-Exchange Approximation. *Phys. Rev. A: At., Mol., Opt. Phys.* **1981**, *24*, 2473−2480.
(48) Takatsuka, K.; McKoy, V. Theory of Electronically Inelastic Scattering of Electrons by Molecules. *Phys. Rev. A: At., Mol., Opt. Phys.* **1984**, *30*, 1734−1740.
(49) Bachelet, G. B.; Hamann, D. R.; Schülter, M. Pseudopotentials That Work: From H to Pu. *Phys. Rev. B: Condens. Matter Mater. Phys.* **1982**, *26*, 4199−4228.
(50) da Costa, R. F.; Varella, M. T. d. N.; Bettega, M. H. F.; Lima, M. A. P. Recent Advances in the Application of the Schwinger Multichannel Method with Pseudopotentials to Electron-Molecule Collisions. *Eur. Phys. J. D* **2015**, *6*, 159.
(51) *NIST Chemistry WebBook*, DOI: 10.18434/T4D303.
(52) Christophorou, L. G. *Adv. Electron. Electron Phys.* **1978**, *46*, 55.
(53) Meißner, R.; Feketeová, L.; Bayer, A.; Postler, J.; Limão-Vieira, P.; Denifl, S. Positive and Negative Ions of the Amino Acid Histidine Formed in Low-Energy Electron Collisions. *J. Mass Spectrom.* **2019**, *54*, 802−816.

https://doi.org/10.1021/jasms.1c00057
J. Am. Soc. Mass Spectrom. 2021, 32, 1459−1468